RESEARCH ARTICLE

Key Points:
- High-frequency energy release process is retrieved for an aftershock sequence
- Apply an envelope inversion to the aftershock sequence
- The energy release follows a power law decay after 40 s

Imaging the high-frequency energy radiation process of a main shock and its early aftershock sequence: The case of the 2008 Iwate-Miyagi Nairiku earthquake, Japan

Kaoru Sawazaki[1] and Bogdan Enescu[2]

[1]National Research Institute for Earth Science and Disaster Prevention, Tsukuba, Japan, [2]University of Tsukuba, Tsukuba, Japan

Abstract To understand the energy release process that operates at the end of the main shock rupture and start of the aftershock activity, we propose an inversion method that uses continuous high-frequency seismogram envelopes of the main shock and early aftershocks (i.e., events that occur at short times after the main shock). In our approach, the aftershock sequence is regarded as a continuous energy release process, rather than a discrete time series of events. To correct for the contribution of coda wave energy excited by multiple scattering, we use the theoretical envelope synthesized on the basis of the radiative transfer theory as a Green's function. The site amplification factors are corrected considering the conservation of energy flux and using the coda normalization method. The inverted temporal energy release rate for the 2008 M_W 6.9 Iwate-Miyagi Nairiku earthquake, Japan, decays following $t^{-1.1}$, at the lapse time t of 40–900 s after the main shock origin time. This exponent of the decay rate is similar to the p value of the modified Omori law. The amount of estimated energy release is consistent with that calculated from the magnitude listed in the aftershock catalog. Although the uncertainty is large, the location of large energy release at the lapse times of 40–900 s approximately overlaps to that of the aftershocks, which surrounds the large energy release area during the main shock faulting. The maxima of the energy release rate normalized by the average decay rate distributes following a power law, similar to the Gutenberg-Richter law.

1. Introduction

The early part of an aftershock sequence holds valuable information about the underlying mechanisms that control the occurrence of aftershocks [e.g., *Dieterich*, 1994]. However, the quantification of events that are occurring immediately after a main shock is a difficult task, as the relatively small early aftershocks are hidden on seismograms by the large-amplitude, lower frequency surface wave of the main shock and, in many cases, overlap one with each other on the recording waveforms [e.g., *Kagan*, 2004]. To overcome this limitation, recent studies [e.g., *Peng et al.*, 2006, 2007; *Enescu et al.*, 2007, 2009] have used high-pass filtered continuous waveform records to detect as many early events as possible. The employed method relies on the careful inspection of filtered waveform data and can determine the origin time and magnitude of the detected early events well. Another approach, known as the Matched Filter Technique, uses the waveforms of already well-located earthquakes as templates to search for other unreported similar nearby events [e.g., *Peng and Zhao*, 2009; *Lengliné et al.*, 2012]. This method has the advantage of being able to determine the location of previously undetected earthquakes, besides their origin time and magnitude.

Although these waveform-based techniques improve the early aftershock catalog dramatically, there are still limitations in their detection capability, which are mainly due to the high-frequency coda wave of the main shock that hinders aftershock detection. For example, *Enescu et al.* [2009] reported that the c value of the modified Omori law [*Utsu*, 1961], which expresses the time interval between the main shock and the onset of the power law decay of aftershocks, could be of less than 1–2 min for several major Japanese inland earthquakes. However, the data within 1 min from the main shock are dominated by the coda waves, which cannot be completely removed.

For high frequencies, the backprojection method has also been widely applied to locate main shock and aftershocks because of its convenience [e.g., *Ishii et al.*, 2005; *Kiser and Ishii*, 2013]. However, the propagation
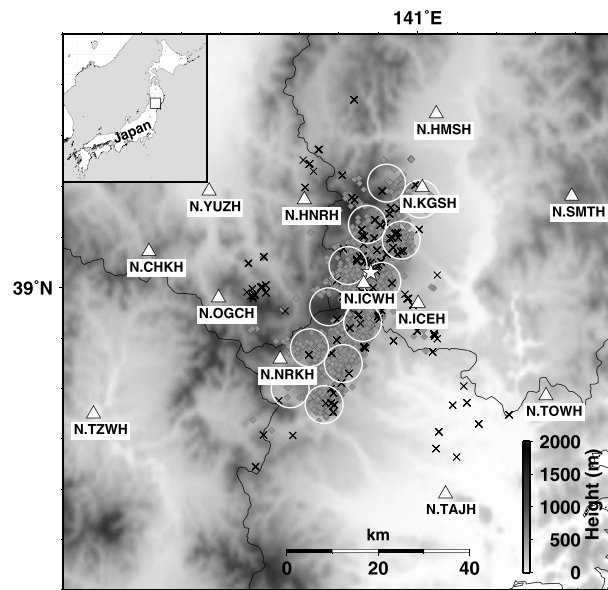
Figure 1. Location of the aftershocks (diamonds) occurring within 1 month after the 2008 Iwate-Miyagi Nairiku earthquake and the earthquakes (crosses) used for the MLTWA and the site correction. The used Hi-net and colocated KiK-net stations are shown by white triangles together with their naming code. White circles represent the spatial grid nodes (subfault) used in the envelope inversion. The star represents the rupture initiation point of the main shock. The borders of governmental prefectures are drawn by black curves. The study area is indicated by the rectangle in the inset map.

effect is usually not effectively corrected in this method, and to understand the physical meaning of the projected image is not straightforward.

Based on the above considerations, we develop an envelope inversion technique to retrieve the high-frequency energy release by early aftershocks and apply it to the continuous records of the 2008 M_W 6.9 Iwate-Miyagi Nairiku earthquake, Japan (hereafter, we refer to this earthquake as the "main shock"), in the frequency range of 1–16 Hz. The envelope inversion has been effectively used for the analysis of high-frequency (>1 Hz) energy release process of large earthquakes [e.g., *Gusev and Pavlov*, 1991; *Kakehi and Irikura*, 1996; *Nakahara et al.*, 1998] and has provided important constraints for understanding the physical mechanisms of the earthquake source [e.g., *Nakahara*, 2008]. This technique should be applicable not only to the study of energy release during large earthquakes but also to investigate other types of energy excitation processes such as aftershocks, earthquake swarms, volcanic and nonvolcanic tremors, and so on. Different from the Matched Filter Technique, the envelope inversion method does not require template events.

In this study, we use continuous seismogram records of Hi-net (high-sensitivity seismograph network Japan) and strong motion records of KiK-net (a strong motion seismograph network in Japan) operated by NIED (National Research Institute for Earth Science and Disaster Prevention) for the detection of energy release process of the main shock and early aftershocks. To model the coda wave energy due to multiple scattering, we use the seismogram envelopes synthesized on the basis of the radiative transfer theory as the envelope Green's function. The scattering coefficient and the intrinsic Q factor used for the envelope synthesis are estimated through the multiple lapse time window analysis (MLTWA). The site amplification factor is also estimated considering the conservation of energy flux and using the coda normalization method. The data processing and the envelope inversion technique are explained in sections 2 and 3, respectively. The performance of the envelope inversion is discussed in section 4. The characteristics of the inverted energy release process are explained in section 5 and discussed in detail in section 6.

2. Data

2.1. Processing of Hi-net Records

Hi-net is the nationwide seismograph network operated by NIED. Figure 1 shows the location of 13 Hi-net stations (triangles) used in the analysis and the aftershock epicenters (gray diamonds) for events with M_J larger than 2 detected within 1 month after the main shock, where M_J is the JMA (Japan Meteorological Agency) magnitude. Each Hi-net station is equipped with a three-component velocity seismometer, which is installed at the bottom of a borehole, at depths greater than 100 m. The electric signal is digitized with a 27 bits resolution and 100 Hz sampling frequency, and the frequency response of the recording system is almost flat from 2 to 20 Hz. The data are continuously recorded and transferred to NIED in real time. The details of the Hi-net acquisition system are summarized by *Obara et al.* [2005].

After correcting for the frequency response, we apply a band-pass filter to the original records using four different frequency bands of 1–2 Hz, 2–4 Hz, 4–8 Hz, and 8–16 Hz. Then we multiply the mass density ρ of
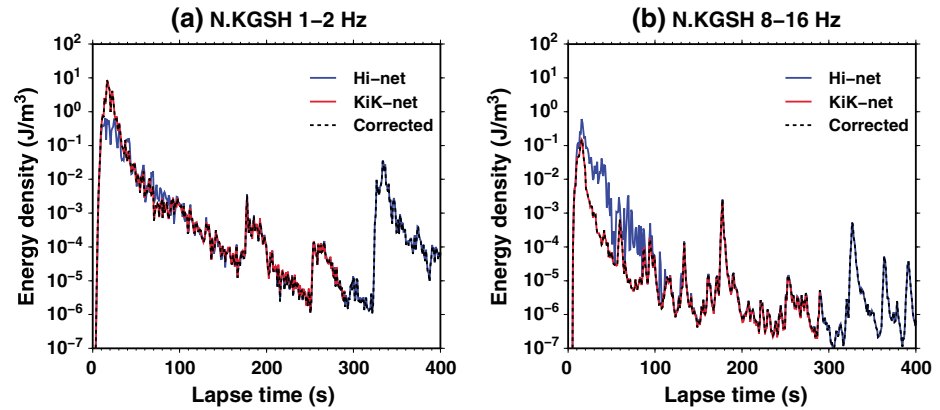
Figure 2. Seismogram envelope of the main shock in the frequency ranges of (a) 1–2 Hz and (b) 8–16 Hz recorded by Hi-net (blue curves) and KiK-net (red curves) sensors at station N.KGSH (KiK-net code: IWTH24). The corrected envelope is shown as a dashed curve. The KiK-net record ends at 291 s because it was recorded in event trigger mode.

2800 kg/m^3 to the squared sum of the three-component velocities to obtain the record of energy density. Finally, the record is smoothed and resampled using a $\Delta t = 1$ s interval.

2.2. Correction for the Saturated Hi-net Record

Shiomi et al. [2005] reported two types of amplitude saturation for the Hi-net recording system. One is the maximum velocity of 4 cm/s, which is due to a limit value of the input voltage that the analog to digital converter can record. Another is the maximum displacement of 0.1 cm and 0.25 cm for the horizontal and vertical components, respectively, which is due to the limitation of stroke amplitude of the seismograph pendulum. In the case of a large displacement, the pendulum is suddenly forced to change its moving direction, and consequently, a spiky high-frequency noise is generated. As a result, the signal recorded during a strong ground motion underestimates and overestimates at the low- and high-frequency components, respectively. Most of the Hi-net records used for our analysis are saturated during the strong ground motion by the Iwate-Miyagi Nairiku earthquake. The significant features of the strong motion record of this earthquake are summarized by *Aoi et al.* [2008].

To correct for the saturation in the Hi-net waveforms, we use the strong motion seismograms recorded by the KiK-net sensors, which are colocated with the Hi-net sensors. Since the KiK-net records are originally accelerograms, we integrate them once to velocity and apply the same processing that is performed for the Hi-net records. We use the KiK-net records for the first 150 s from the main shock origin time and use the Hi-net records after 160 s. From 150 s to 160 s, the relative weight of the two records changes linearly. Figure 2 shows an example of 1–2 Hz and 8–16 Hz seismogram envelopes for the main shock recorded by Hi-net (blue curves) and KiK-net (red curves) sensors at N.KGSH (or IWTH24, using the KiK-net naming code) station. The dashed curves are the corrected envelopes. There are biases in the early part of the Hi-net record; the 1–2 Hz and 8–16 Hz envelopes are underestimated and overestimated, respectively. These biases are properly corrected by using the KiK-net record. We have checked that the Hi-net and KiK-net records are almost the same after 160 s for all the 13 stations used in this study.

3. Method

Considering the incoherent propagation of the high-frequency (>1 Hz) seismic wave, we synthesize the theoretical seismogram envelope E by convolving the energy release function W, the envelope Green's function G, and the site amplification factor S. This envelope is written as

$$E_{i,j} \approx S_i \sum_{l=1}^{l\max} G_{i,j,k(l),l} W_{k(l),l}, \tag{1}$$

where i, j, k, and l are the stations, the time nodes for gridding the observed envelope, the spatial nodes for gridding the fault (white circles in Figure 1), and the time nodes for gridding the energy release function,

respectively. We assume that the energy is released at only one subfault $k(l)$ at each time node l. In other words, we estimate the "centroid" of the energy release at each time step. The number of stations i_{max} and that of time nodes j_{max} are 13 and 1000, respectively.

We set $l_{max} = 900$ and a sampling interval of 1 s. Considering the distribution of aftershocks and the fault model proposed by *Ohta et al.* [2008], we set $k_{max} = 12$ subfaults on the fault plane at 10 km interval, with the strike, dip, and rake angles of 205°, 35°, and 95°, respectively. Apparently, the subfault size of 10 km seems to be too large for locating aftershocks. However, we emphasize that our motivation is not to locate each "discrete" aftershock separately but to locate the centroid of the energy release at each time step. *Gusev and Pavlov* [1991] introduced a similar concept to estimate the centroid of high-frequency energy radiation from the 1978 Miyagi-Oki earthquake, Japan. Also, we note that the spatial resolution of our envelope inversion is not better than 10 km (as discussed in section 4), and modeling using a smaller subfault size and more complex fault geometry does not improve the robustness of the inversion.

3.1. Envelope Green's Function

To account for the multiple scattering of S wave energy for a point-like impulsive source, we use the equation proposed by *Paasschens* [1997] as the envelope Green's function G. The equation is given by

$$
\begin{aligned}
G(r,f,t) &\approx \frac{1}{4\pi V_S r^2} \delta\left(t - \frac{r}{V_S}\right) \exp\left\{-\left[g_0(f)V_S + 2\pi Q_i^{-1}(f)f\right]t\right\} \\
&+ \frac{\left[1 - r^2/(V_S t)^2\right]^{1/8}}{\left[4\pi V_S t/(3g_0(f))\right]^{3/2}} \exp\left\{-\left[g_0(f)V_S + 2\pi Q_i^{-1}(f)f\right]t\right\} \\
&\cdot M\left[g_0(f)V_0 t\left(1 - \frac{r^2}{V_S^2 t^2}\right)^{3/4}\right] H\left(t - \frac{r}{V_S}\right)
\end{aligned}
\tag{2}
$$

$$M(x) \approx \exp(x)\sqrt{1 + 2.026/x}$$

where r, V_S, g_0, and Q_i^{-1} are the source-receiver distance, the background S wave velocity, the (isotropic) scattering coefficient, and the inverse of intrinsic Q factor, respectively. The equation (2) is an approximation of the exact solution of the radiative transfer equation for a point isotropic source in a 3-D scattering medium, which was solved by *Zeng et al.* [1991]. Because the excitation of P wave energy is much smaller than that of S wave energy for a double-couple source (1/23.4 in a Poisson medium), we neglect the contribution of P wave energy throughout the analysis. Equation (2) was used for mapping of g_0 and Q_i^{-1} in Kamchatka [*Abubakirov*, 2005] and Japan [*Carcolé and Sato*, 2010].

We perform the multiple lapse time window analysis (MLTWA) proposed by *Fehler et al.* [1992] to estimate g_0 and Q_i^{-1} in the target area. We separate the envelope record into three time windows: -1–15 s, 15–30 s, and 30–45 s relative to the S wave onset time and estimate the best fit parameters that describe the energy balance among the three time windows. A grid search for g_0 and Q_i^{-1} is performed with the grid interval of $\Delta g_0 = 0.001$ km^{-1} and $\Delta Q_i^{-1} = 0.0001$ in each frequency range. The crosses in Figure 1 indicate the location of earthquakes used for the MLTWA. These earthquakes are located at depths shallower than 15 km, which corresponds to the depth limit of the main shock rupture zone, and occurred between January 2003 and December 2008. The aftershocks occurring within 2 weeks after the main shock (14–27 June 2008) are excluded since many event records are overlapping each other.

Figure 3 shows the error contour of the grid search for g_0 and Q_i^{-1} in the frequency ranges of 1–2 Hz, 2–4 Hz, 4–8 Hz, and 8–16 Hz. The black circles and the shaded zones indicate the best fit values and the areas of 95% confidence, respectively. The best fit parameters are summarized in Table 1 with the 95% confidence interval determined from the shaded zones in Figure 3. For both g_0 and Q_i^{-1}, their uncertainties are larger for the lower frequencies, probably because of the excitation of surface waves which are neglected in the body wave scattering regime. Our estimated g_0 is generally larger than that of *Carcolé and Sato* [2010] for the same region. Note, however, that our study uses the earthquakes with the depth shallower than 15 km, while *Carcolé and Sato* [2010] use the events located down to 40 km depth. Since the energy of shallow earthquakes tends to be trapped by the low-velocity sediment and the apparent envelope decay of such
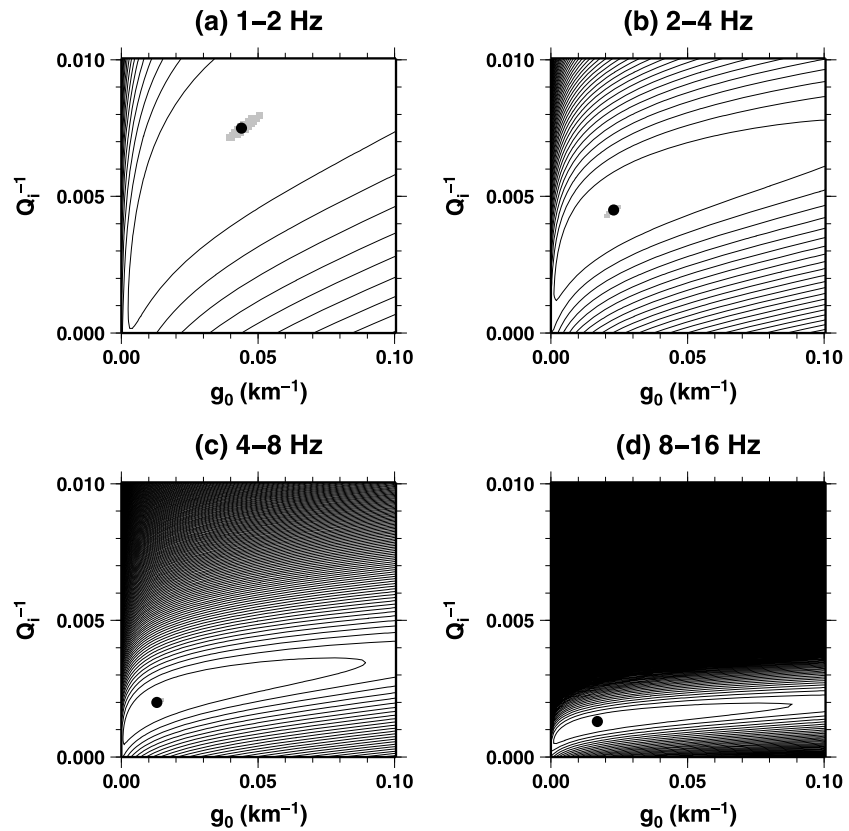
Figure 3. Error contours of the grid search for g_0 and Q_i^{-1} in the frequency ranges of (a) 1–2 Hz, (b) 2–4 Hz, (c) 4–8 Hz, and (d) 8–16 Hz. The best fit parameters and the 95% confidence area are shown by the black circles and the gray zones, respectively. The contours are drawn at a 10% residual interval.

shallow events becomes slow, the g_0 value estimated in this study might become relatively larger. The estimation of g_0 and Q_i^{-1} does not change systematically before and after the main shock, which confirms the temporal stability of these parameters.

The background V_S for each subfault-station pair is estimated using the S wave traveltime of small earthquakes (crosses in Figure 1). We assume V_S at each station i and earthquake n as

$$V_{Si,n} = A_i \cdot \text{Epi}_{i,n} + B_i \cdot \text{Dep}_n + C_i, \tag{3}$$

where Dep and Epi are the source depth and epicentral distance, respectively. We consider that this formula is acceptable as a first approximation since the velocity of the crust varies with depth and the S wave propagates through the deeper zone as the hypocentral depth and epicentral distance increase. The V_S and its variance σ_{VS}^2 are measured as $V_S = \sqrt{\text{Epi}^2 + \text{Dep}^2}/T$ and $\sigma_{VS}^2 = (\text{Epi}^2 + \text{Dep}^2)\delta T^2/T^4$, where T and δT are the S wave traveltime and its measurement error, respectively. We assume $\delta T = 0.5$ s because the envelope is

Table 1. The Estimated Scattering Coefficient g_0 and the Inverse of the Intrinsic Factor Q_i^{-1} With the 95% Confidence Interval

	1–2 Hz	2–4 Hz	4–8 Hz	8–16 Hz
g_0 (10^{-3} km^{-1})	44 ± 6	23 ± 3	13 ± 2	17 ± 1
Q_i^{-1} (10^{-4})	75 ± 5	45 ± 2	20 ± 1	13 ± 1

Table 2. The Estimated Parameters A, B, and C With the 95% Confidence Interval

V_S (km/s)	A (10^{-3} s^{-1})	B (10^{-3} s^{-1})	C (km/s)
N.CHKH	-0.08 ± 0.24	27.5 ± 1.0	3.20 ± 0.01
N.HMSH	-0.06 ± 0.24	7.89 ± 1.28	3.24 ± 0.02
N.HNRH	1.56 ± 0.42	49.6 ± 2.0	2.79 ± 0.02
N.ICEH	11.2 ± 1.0	20.8 ± 1.9	2.62 ± 0.03
N.ICWH	5.55 ± 1.43	32.9 ± 3.1	2.74 ± 0.04
N.KGSH	4.28 ± 0.32	6.38 ± 1.23	2.84 ± 0.02
N.NRKH	10.2 ± 0.7	80.0 ± 2.8	2.23 ± 0.02
N.OGCH	1.49 ± 0.56	35.2 ± 1.6	2.97 ± 0.02
N.SMTH	3.56 ± 0.16	8.16 ± 0.67	3.12 ± 0.01
N.TAJH	5.26 ± 0.24	6.71 ± 1.18	2.84 ± 0.01
N.TOWH	5.70 ± 0.15	14.2 ± 0.6	2.90 ± 0.01
N.TZWH	2.61 ± 0.24	11.0 ± 1.0	3.03 ± 0.01
N.YUZH	0.26 ± 0.18	41.2 ± 1.0	2.94 ± 0.01

resampled every 1 s and the picking error of the S wave onset time is much smaller than 1 s, in general. The coefficients A, B, and C are estimated by solving the least squares inversion given by

$$\mathbf{M}_i = \begin{bmatrix} A_i \\ B_i \\ C_i \end{bmatrix} = \left[\mathbf{G}_i^T \operatorname{cov} \mathbf{D}_i^{-1} \mathbf{G}_i \right]^{-1} \mathbf{G}_i^T \operatorname{cov} \mathbf{D}_i^{-1} \mathbf{D}_i$$

$$\operatorname{cov} \mathbf{M}_i = \left[\mathbf{G}_i^T \operatorname{cov} \mathbf{D}_i^{-1} \mathbf{G}_i \right]^{-1}$$

$$\mathbf{G}_i \equiv \begin{bmatrix} \text{Epi}_{i,1} & \text{Dep}_1 & 1 \\ \text{Epi}_{i,2} & \text{Dep}_2 & 1 \\ \vdots & \vdots & \vdots \\ \text{Epi}_{i,N} & \text{Dep}_N & 1 \end{bmatrix}, \quad \mathbf{D}_i \equiv \begin{bmatrix} V_{Si,1} \\ V_{Si,2} \\ \vdots \\ V_{Si,N} \end{bmatrix}, \quad \operatorname{cov} \mathbf{D}_i \equiv \begin{bmatrix} \sigma^2_{VSi,1} & 0 & 0 & 0 \\ 0 & \sigma^2_{VSi,2} & 0 & 0 \\ 0 & 0 & \ddots & \vdots \\ 0 & 0 & \cdots & \sigma^2_{VSi,N} \end{bmatrix}, \tag{4}$$

where $\mathbf{M}$, $\operatorname{cov}\mathbf{M}$, $\mathbf{G}$, $\mathbf{D}$, and $\operatorname{cov}\mathbf{D}$ represent the model parameter vector, covariance matrix for the model parameters, kernel matrix, data vector, and covariance matrix for the data, respectively. The values A, B, and C at each station together with their 95% confidence interval are summarized in Table 2.

An example of the observed and synthesized envelopes for the best fit parameters is shown in Figure 4. The synthesized envelope is adjusted to the observed counterpart at 50–60 s, for comparison purposes. The coda part of the synthesis fits well to the observed envelope in the logarithmic scale, while the signal around the ballistic S wave energy arrival (at about 10–20 s) is poorly fitted. This misfit is caused by the dominance of forward scattering around the ballistic arrival [*Sato*, 1989; *Saito et al.*, 2002] and the anisotropic radiation pattern of the double-couple source

Figure 4. Example of the observed envelope for an M_J 3.9 earthquake occurring on 15 September 2008 recorded at station N.KGSH (solid curves) and the synthesized envelope for the best fit parameters of g_0 and Q_i^{-1} (dashed curves). The envelopes in the frequency ranges of 1–2 Hz, 2–4 Hz, 4–8 Hz, and 8–16 Hz are drawn by red, orange, green, and blue curves, respectively. The dashed rectangle represents the time window used for parameter estimation.

Table 3. The Estimated Site Amplification Factor S With the Logarithmic 95% Confidence Interval in the Bracket

S	1–2 Hz	2–4 Hz	4–8 Hz	8–16 Hz
N.CHKH	0.48 (1.11)	0.43 (1.06)	0.46 (1.17)	0.77 (1.19)
N.HMSH	88.2 (1.52)	75.4 (1.10)	57.6 (1.06)	55.7 (1.11)
N.HNRH	2.40 (1.10)	3.15 (1.07)	4.73 (1.10)	4.73 (1.10)
N.ICEH	33.2 (1.24)	15.0 (1.14)	10.4 (1.10)	6.55 (1.10)
N.ICWH	2.11 (1.12)	2.70 (1.11)	5.47 (1.07)	8.74 (1.07)
N.KGSH	86.4 (1.38)	27.1 (1.14)	16.5 (1.08)	11.6 (1.09)
N.NRKH	1.88 (1.70)	0.84 (1.23)	0.74 (1.08)	0.84 (1.07)
N.OGCH	2.31 (1.17)	2.06 (1.10)	2.20 (1.20)	2.34 (1.16)
N.SMTH	1.43 (1.12)	5.57 (1.09)	6.72 (1.08)	6.49 (1.09)
N.TAJH	10.8 (1.39)	10.9 (1.10)	10.1 (1.09)	8.06 (1.09)
N.TOWH	1.24 (1.08)	6.59 (1.08)	6.06 (1.07)	9.95 (1.10)
N.TZWH	1.34 (1.21)	1.09 (1.11)	1.04 (1.12)	0.76 (1.14)
N.YUZH	3.75 (1.19)	3.00 (1.09)	3.09 (1.10)	2.46 (1.15)

[e.g., *Sawazaki et al.*, 2011], which are not reflected in equation (2). The synthesized envelope is slightly underestimated at the lapse times of over 60 s. This misfit is attributed to both the nonisotropic scattering and the depth dependence of the scattering coefficient [*Gusev*, 1995; *Calvet and Margerin*, 2013].

3.2. Correction for the Site Amplification

We estimate the site amplification factor by considering global and local correction factors; the global factor is applied uniformly to all stations, while the local factor is applied individually to each station.

The global factor corrects for the free surface and the 1-D velocity structure, which are common for all used stations. Since the Hi-net sensor is installed at the borehole bottom, the waveform record contains an incident signal from the subsurface and a signal reflected on the free surface that propagates incoherently. Therefore, a multiplication factor of 2 must be considered. In addition, we have to consider the conservation of energy flux between the depths of hypocenters and Hi-net sensors. Averaging the V_S at the installed depth of 13 Hi-net sensors from the well-logging data provided by NIED, we obtain $V_{Ssite} = 1.48$ km/s. The average V_S at the source is estimated from the S wave traveltime of small earthquakes as $V_{Ssource} = 3.28$ km/s. As a result, the global site amplification factor is evaluated as $2V_{Ssource}/V_{Ssite} = 4.43$.

The energy of the multiple scattered wave recorded at the same lapse time does not vary with the source-receiver path. Using this property of the scattered energy, we estimate the local site amplification factor through the coda normalization method [*Phillips and Aki*, 1986]. The logarithmic average of coda energy for 13 Hi-net stations at 50–60 s after the source origin time is adjusted to the global site amplification factor. The local site amplification factor is expressed as the ratio between the coda wave energy at a certain station and the average coda energy.

Table 3 shows the estimated site amplification factors combining the global and local factors, with the logarithmic 95% confidence interval in brackets. The site amplification factor varies with stations especially at the lower frequencies. This wide variety in the amplification factor originates from the diverse geology around stations as well as from the excited wave type. Surface waves may be effectively excited in the basin region surrounding stations N.HMSH and N.KGSH (see the topography in Figure 1) at 1–2 Hz, at which the large amplifications are estimated. According to *Takemoto et al.* [2012], the site amplification factors of K-NET and KiK-net stations in Japan distribute within the range of 20 dB (factor of 100), for frequencies of 1–2 Hz.

3.3. Iterative Grid Search Inversion

We use an iterative grid search technique for the inversion of spatiotemporal energy release. We first set the initial energy release function as

$$W_{k(l),l} = 10^{20}(J) \quad \text{for} \quad l = 1$$
$$= 0(J) \qquad \text{for} \quad l > 1 \tag{5}$$

and search $\bar{k}(1)$ that minimizes

$$\text{err1} = \sum_{i=1}^{i\max} \left\{ \log_{10}\left[O_{i,1 + T(i,k(1))/\Delta t}\right] - \log_{10}\left[E_{i,1 + T(i,k(1))/\Delta t}\right] \right\}^2, \tag{6}$$

where O and E are the observed and synthesized envelopes calculated from equation (1) and $T(i, k(1))$ is the S wave traveltime from the subfault $k(1)$ to the station i. By equation (6), we account for the spatial distribution of ballistic S wave energy only because scattered waves do not include the information of source location. The choice of initial energy release $W_{k(1),1}$ is arbitrary, but it should be large enough compared to the actual energy release. After searching for $\bar{k}(1)$, we calculate $\overline{W}_{\bar{k}(1),1}$ using

$$\overline{W}_{\bar{k}(1),1} = W_{\bar{k}(1),1} 10^{\frac{1}{i\max}\sum_{i=1}^{i\max}\left\{\log_{10}\left[O_{i,1+T(i,\bar{k}(1))/\Delta t}\right] -, \log_{10}\left[E_{i,1+T(i,\bar{k}(1))/\Delta t}\right]\right\}}. \tag{7}$$

Then we renew the energy release function as

$$\begin{aligned} W_{k(l),l} &= \overline{W}_{\bar{k}(1),1}(\text{J}) &&\text{for}\quad l = 1 \\ &= 10^{20}(\text{J}) &&\text{for}\quad l = 2 \\ &= 0(\text{J}) &&\text{for}\quad l > 2 \end{aligned} \tag{8}$$

and search for the best fit $\bar{k}(2)$ and $\overline{W}_{\bar{k}(2),2}$ using the equations (6) and (7) for $l = 2$. By iterating the calculation steps above, we obtain $\bar{k}(l)$ and $\overline{W}_{\bar{k}(l),l}$ for all the time nodes l. After reaching $l = l_{\max}$, we calculate

$$\text{err2} = \sum_{i=1}^{i\max}\sum_{j=1}^{l\max}\left\{\log_{10}\left[O_{i,j}\right] - \log_{10}\left[E_{i,j}\right]\right\}^2 \tag{9}$$

to check the overall fitness of the envelope.

Then we return to $l = 1$ again and search $\bar{k}(l)$ and $\overline{W}_{\bar{k}(l),l}$ using equations (6) and (7). In this second running, we use

$$W_{k(l),l} = \overline{W}_{\bar{k}(l),l}(\text{J}) \qquad \text{for all } l \tag{10}$$

as the initial energy release function instead of equation (5) and renew $\overline{W}_{\bar{k}(l),l}$ iteratively. The iterative process stops when the reduction rate of err 2 becomes less than 0.1% before and after the iteration.

The adopted inversion scheme effectively utilizes the causality relation between the timing of energy release and recording of the released energy, which reduces the computation time drastically. Although this scheme does not necessarily search the best solution, it is fast and robust. For most trials, we need less than 10 iterations for the convergence of err 2 and need just a few tens of seconds to obtain the final result using an Intel Xeon 3.33 GHz processor with one core. Note that the L2 norms defined in equations (6) and (9) are calculated for the logarithm of the envelopes because the envelope Green's function is estimated by fitting the logarithmic amplitude of the coda envelope as shown in Figure 4.

4. Synthetic Test

Before applying the envelope inversion to the real data, we test the performance of the inversion scheme proposed in section 3.3. We first produce the artificial envelope by convolving the envelope Green's function using the best fit parameters g_0, Q_i^{-1}, V_S, and S (site amplification factor) to the artificial input energy release function. Then, we invert the synthesized artificial envelope using 50 different envelope Green's functions, where the parameter set of each envelope Green's function is randomly selected within the standard deviations as shown in Tables 1 to 3. Finally, we calculate the average and the standard deviation of the 50 inverted energy release functions and compare them to the input energy release function.

Temporal change in the input (common for 1–2 Hz and 8–16 Hz, as drawn by black curves) and inverted energy release rates are shown in Figure 5a in a log-log scale plot. The red and blue curves represent the ranges of the standard deviation for the 50 inverted energy releases in the frequency ranges of 1–2 Hz and 8–16 Hz, respectively. The synthetic input energy release rate is produced considering the realistic energy release process of the main shock and aftershocks: a large amount of energy is released by the main shock faulting in the first 10 s, and the energy released by the aftershocks decays following the modified Omori law (proportional to $t^{-1.1}$) after that. Several short energy pulses by large aftershocks are excited during the gradual decay. The recovery of the energy release rate is relatively poor at the lapse time range of 10–40 s. The overestimation of the energy release at this lapse time range is attributed to the contamination of
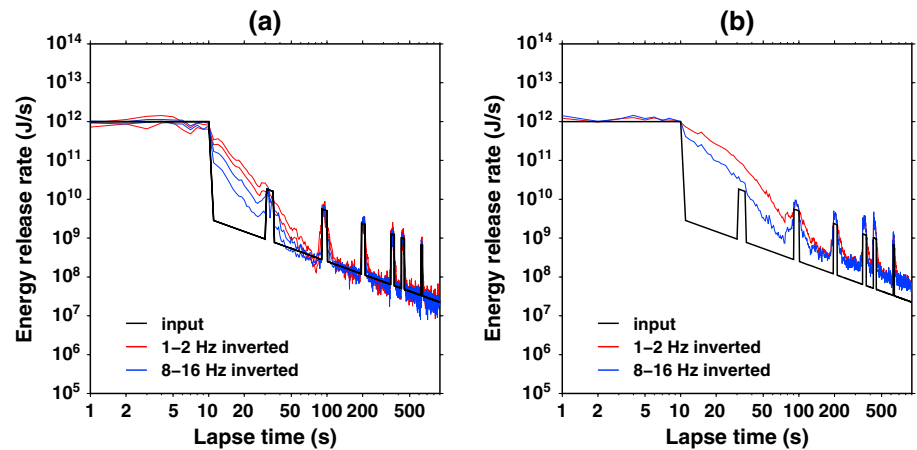
Figure 5. Result of the synthetic test for the temporal change in energy release rate inverted by using (a) randomly selected parameters around the best fit values and (b) best fit parameters except for $g_0 = 0$. The input energy release rate is drawn by the black curve. In Figure 5a, the standard deviation of the inverted energy release rate for 50 random parameter sets is drawn by the red and blue curves for 1–2 Hz and 8–16 Hz, respectively.

scattered wave energy which is not corrected sufficiently in the inversion. The recovery of the energy release rate is better for the higher frequencies because the scattered energy decays more rapidly for the higher frequencies (see Figure 4). After about 40 s, the overall energy release rate is recovered well, and the amplitudes of the short energy pulses are captured well by the inversion. We conclude that our inversion scheme well retrieves the temporal change in energy release unless the energy release rate decreases suddenly by more than one order.

In Figure 5b, we show the same inversion result using the best fit parameters, except that the scattering coefficient is chosen as $g_0 = 0$ for both 1–2 Hz and 8–16 Hz. The inverted energy release rate is overestimated at all the lapse times except for the first 10 s, and the recovery is much worse than the result shown in Figure 5a. Figure 5b demonstrates that all the scattered energies are incorrectly transferred to the released energy because the scattering effect is neglected in the envelope Green's function used for the inversion. From this result, although our inversion scheme may not be perfectly suitable for sudden decrease of energy release rate, it is still much better than other methods that do not correct for the scattered energy.

Figure 6 shows the spatial distribution of input (left columns) and inverted (right columns) energy releases for the same parameters used in the plot of Figure 5a at the lapse time ranges of 0–10 s, 10–40 s, 40–200 s, and 200–900 s. Before the inversion, we assign four subfaults (colored subfaults in the "input" figures) as the candidate for energy radiation in advance. Then, in the inversion, we randomly select one of the four subfaults which releases energy at each time node. The recovery of spatial distribution of energy release is poor at 1–2 Hz (Figure 6a), so our inversion scheme cannot retrieve any spatial information of the energy release in this frequency range. The recovery becomes better as the dominant frequency increases (Figure 6b) except for the lapse time of 10–40 s, at which the scattered energy is contaminated. The major factor of this mislocation is likely related to the validity of the envelope Green's function used in this study. As indicated in equation (6), we search the location of energy radiation by minimizing the squared log residual between the synthesized and observed amplitudes of the ballistic S wave envelope. Since the amplitude of the ballistic S wave is not synthesized correctly as mentioned in section 3.1, we would fail to estimate the energy release location with precision. From this result, we conclude that the spatial resolution of our inversion scheme is not better than 10 km, and basically, the higher frequencies should be used for a plausible interpretation of the inversion result.

5. Result

Figure 7 shows the observed (black curves) and fitted (red curves) seismogram envelopes obtained by the envelope inversion. The energy release by aftershocks is prominent especially at shorter distances and higher
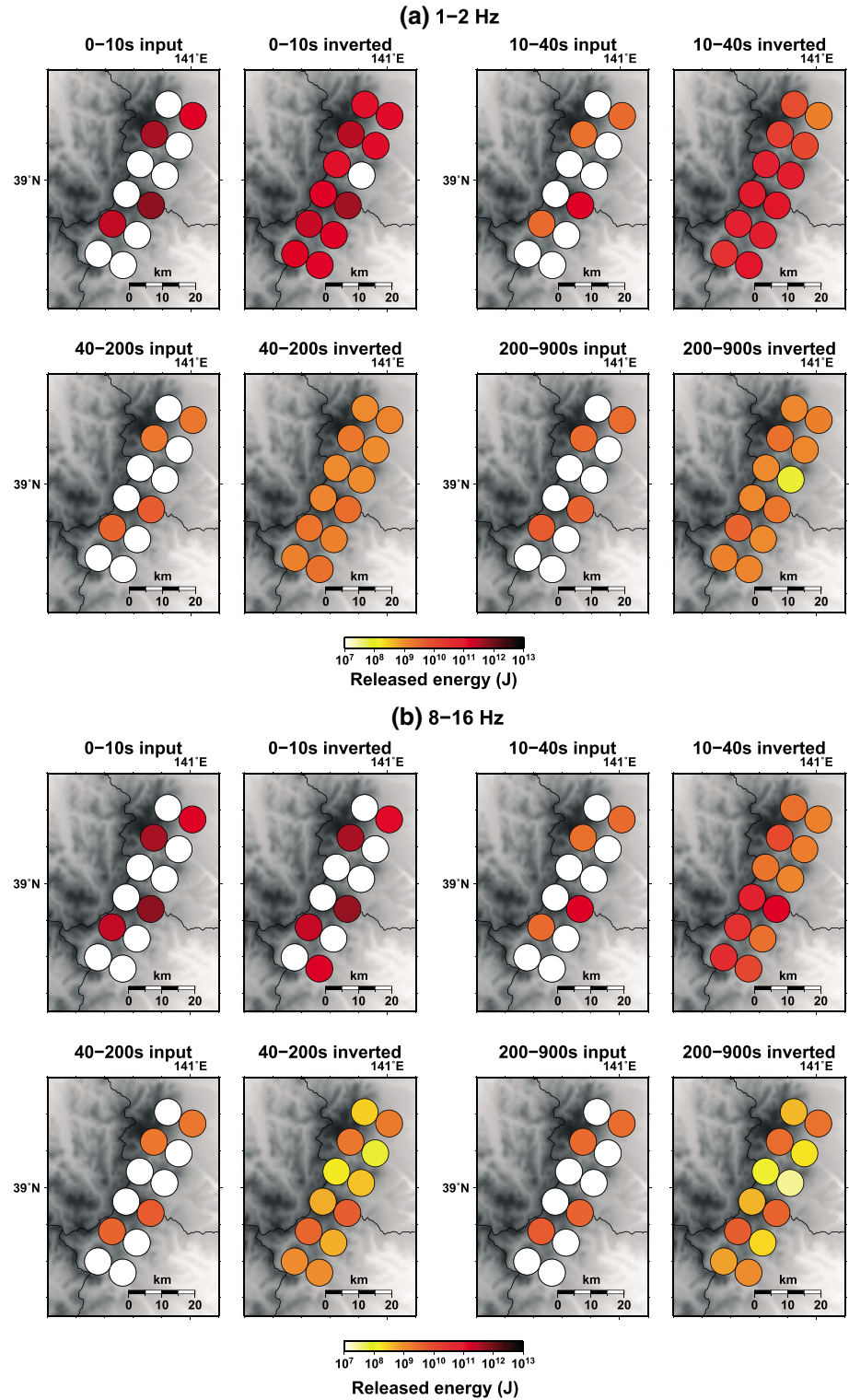
Figure 6. Result of the synthetic test for the spatial distribution of energy release at the lapse time ranges of 0–10 s, 10–40 s, 40–200 s, and 200–900 s in the frequency ranges of (a) 1–2 Hz and (b) 8–16 Hz. The parameters used for the inversion are same to that used for the plot of Figure 5a. The left and right columns for each lapse time and frequency range represent the input and the inverted energy distributions that averaged 50 inversion results, respectively.
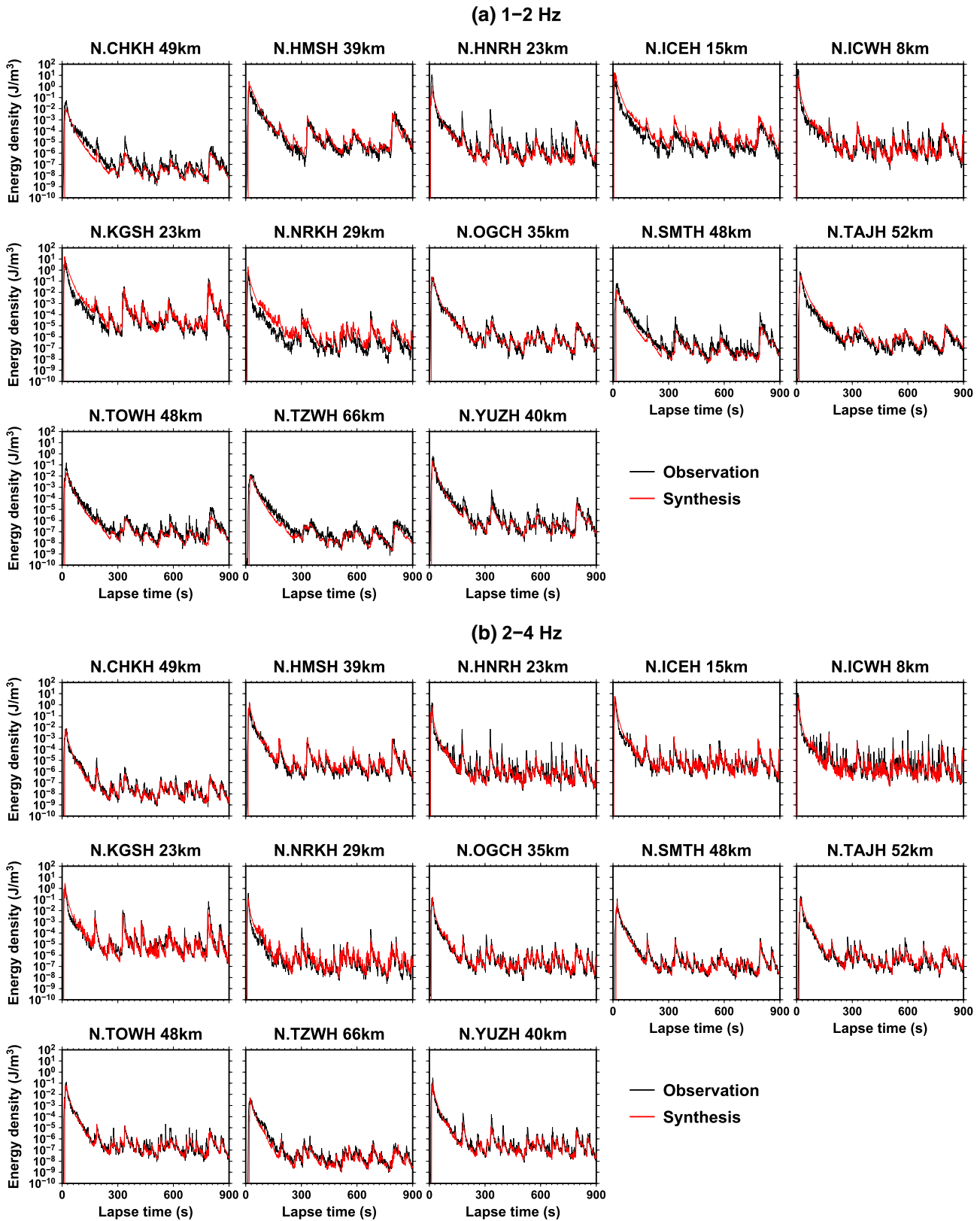
Figure 7. Observed (black curves) and synthesized (red curves) envelopes for the best fit energy release functions in the frequency ranges of (a) 1–2 Hz, (b) 2–4 Hz, (c) 4–8 Hz, and (d) 8–16 Hz. The Hi-net station code name and the distance from the rupture initiation point of the main shock are written on the top of each plot.
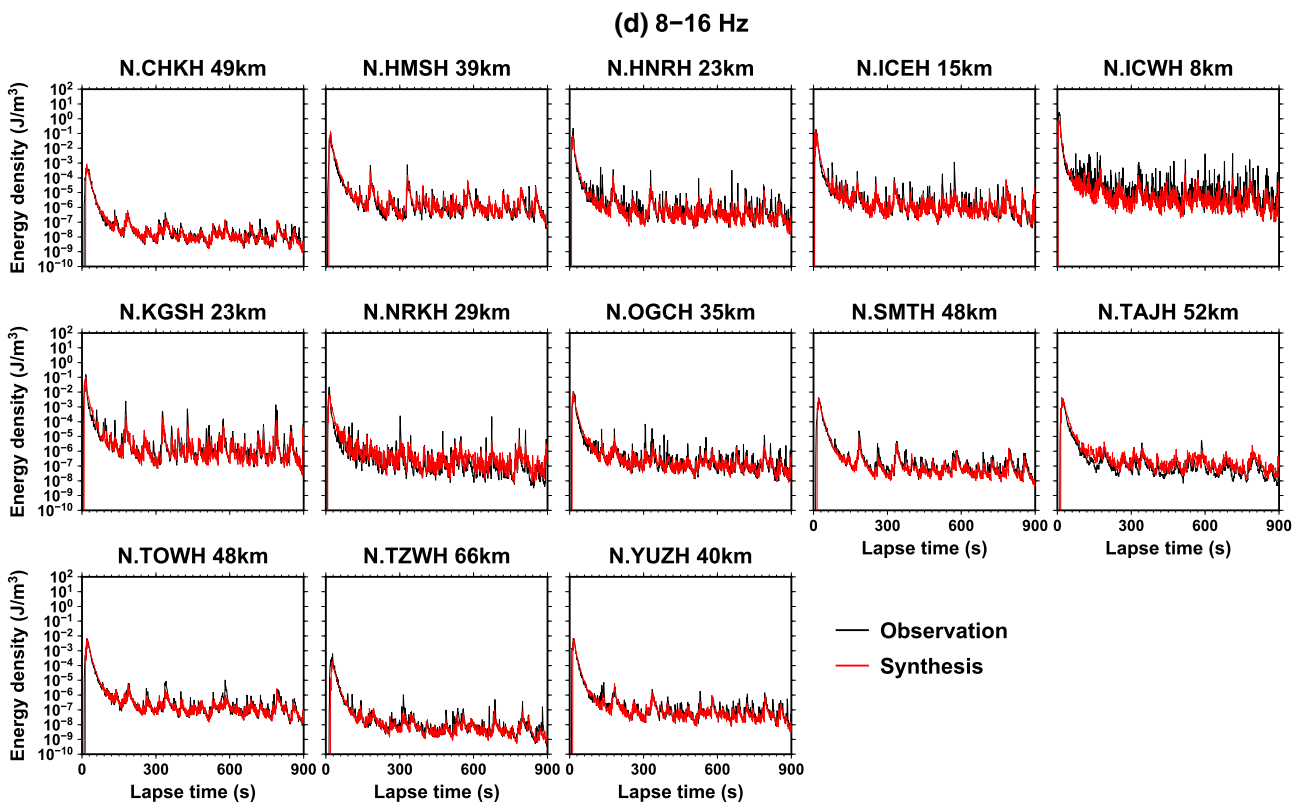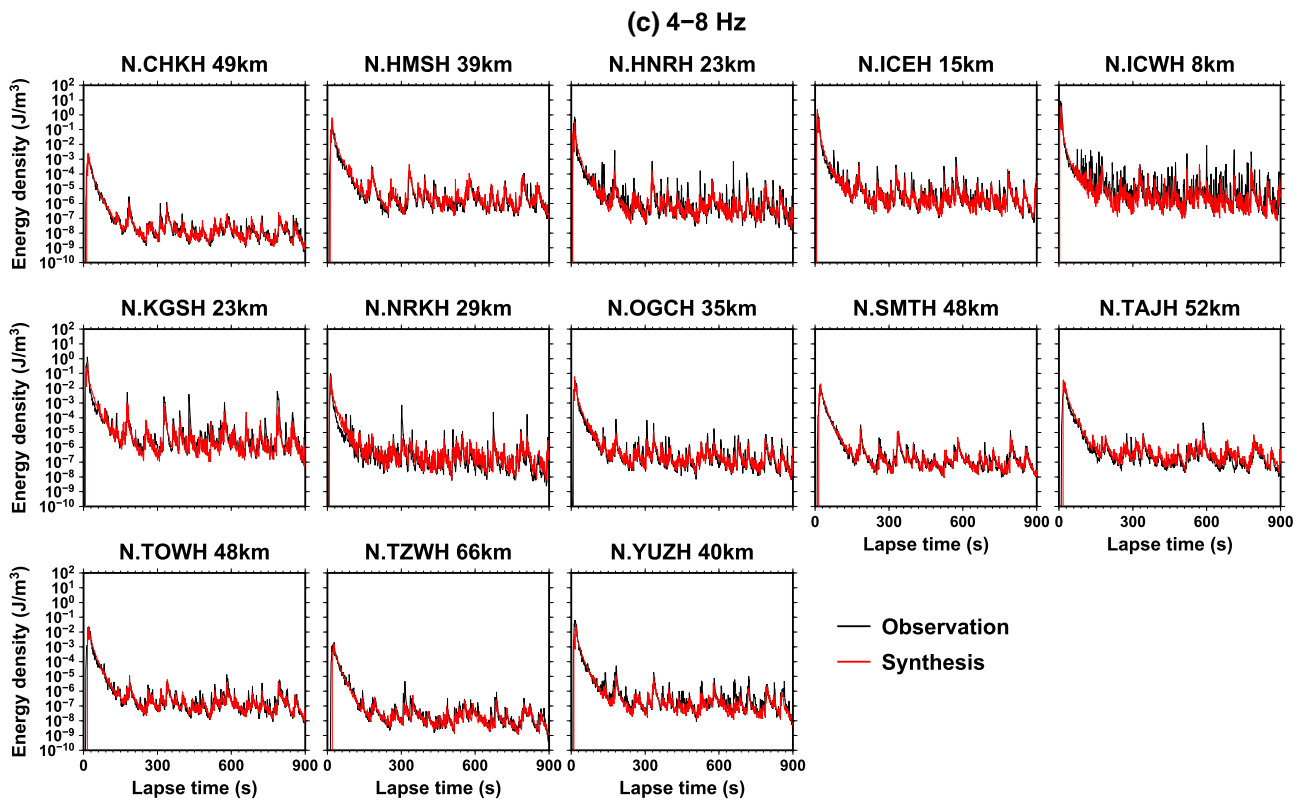
Figure 7. (continued)
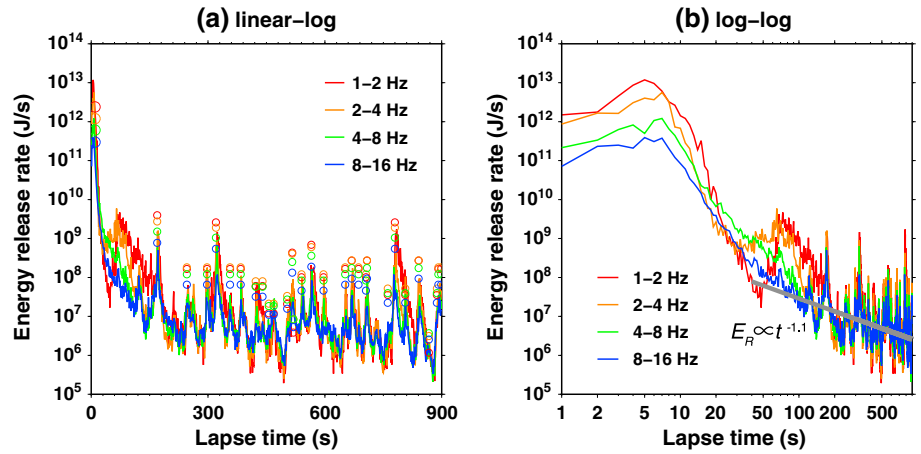
Figure 8. Temporal change in the inverted energy release rate: (a) linear-log and (b) log-log scale plots. The energy release rates in the frequency ranges of 1–2 Hz, 2–4 Hz, 4–8 Hz, and 8–16 Hz are drawn by red, orange, green, and blue curves, respectively. The circles in Figure 8a represent the timing and the amount of energy release by the aftershocks listed in the JMA unified hypocenter catalog. The gray line in Figure 8b represents the regression line fitted to the 8–16 Hz energy release rate at the lapse time range of 40–900 s.

frequencies. The synthesized envelopes capture well both the decay of coda energy in the first tens of seconds and the burst-like energy excitations by the early aftershocks after that. The fitting is not good at some stations especially for the lower frequency ranges, probably due to the contamination of surface waves.

Figures 8a and 8b show the temporal change in the estimated energy release rate plotted in linear-log and log-log scales, respectively. The lapse time of 0–10 s corresponds to the period responsible for the faulting of the main shock. At this lapse time range, the energy release rate is nearly constant in the logarithmic scale. The amount of energy release decreases as the dominant frequency increases because the corner frequency of the M_W 6.9 main shock is much smaller than 1 Hz. After that, the energy release rate decays suddenly at the lapse time range of 10–40 s. Following the result of synthetic test, we think the energy release rate at this lapse time could be overestimated. After 40 s, the burst-like energy release by the early aftershocks becomes dominant. The energy release rate does not vary with frequency significantly at this later lapse times.

The small circles in Figure 8a represent the amount of energy release by the main shock and the aftershocks listed in the JMA unified hypocenter catalog. The amount of energy release is estimated as follows. First, we regard the listed M_J (JMA magnitude) as M_W and convert M_W to the seismic moment M_0 using $\log M_0 = 1.5 M_W + 9.1$ [*Kanamori*, 1977]. Then we calculate the amount of S wave energy release W_{catalog} at the frequencies from f_L to f_H using the omega-square source spectrum [*Aki*, 1967] as

$$W_{\text{catalog}} = \frac{1}{10\pi\rho V_S^5} \int_{f_L}^{f_H} \left| \frac{2\pi f M_0}{1 + (f/f_C)^2} \right|^2 df, \tag{11}$$

where the corner frequency f_C is calculated from the circular crack model [*Eshelby*, 1957; *Brune*, 1970] as

$$f_C = \frac{2.34 V_S}{2\pi} \left[\frac{16\Delta\sigma}{7M_0} \right]^{1/3}. \tag{12}$$

We assume that the stress drop $\Delta\sigma$ is a function of M_0 given by

$$\Delta\sigma = A M_0^B \tag{13}$$

and search the parameters A and B that account for the peaks of the energy release rate. We did not perform an inversion for the estimation of A and B but searched the parameters by trial and error. The circles in Figure 8a are plots for the parameters of $A = 40$ Pa/(Nm)^B and $B = 0.26$ (stress drops of 5.0 MPa and 0.4 MPa for M_W 7 and M_W 4 earthquakes, respectively). The used M_0-$\Delta\sigma$ relationship is consistent with Figure 3b of *Oth et al.* [2010], which examined the scaling properties of Japanese earthquakes. The M_0-$\Delta\sigma$ relationship is still under ongoing discussion [e.g., *Mayeda et al.*, 2005; *Baltay et al.*, 2011], and we do not discuss further about
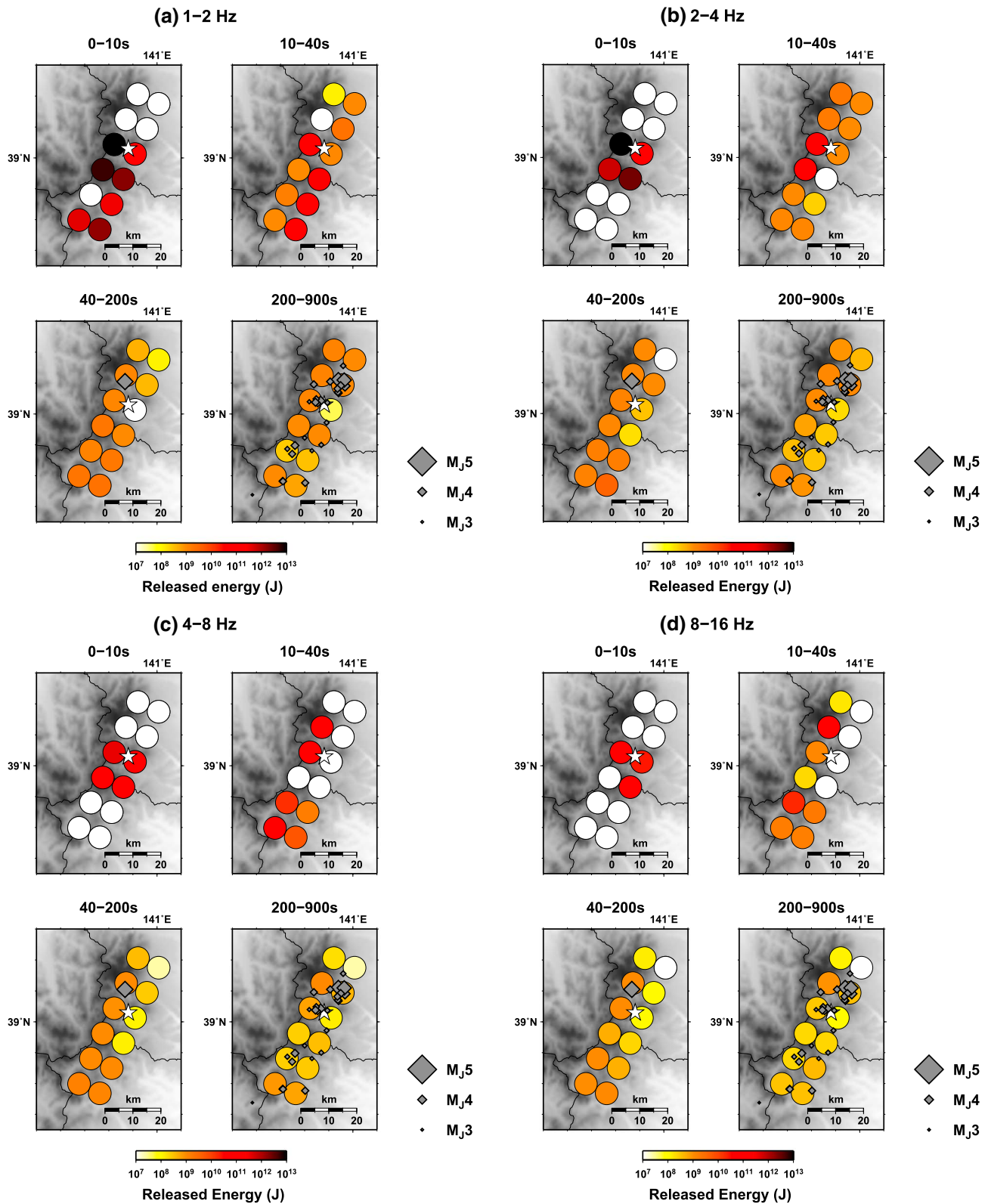
Figure 9. Spatial distribution of the inverted cumulative energy release at the lapse time ranges of 0–10 s, 10–40 s, 40–200 s, and 200–900 s in the frequency ranges of (a) 1–2 Hz, (b) 2–4 Hz, (c) 4–8 Hz, and (d) 8–16 Hz. The stars and diamonds represent the rupture initiation point of the main shock and the location of aftershocks listed in the JMA unified hypocenter catalog, respectively.

this relationship. For the main shock, the calculated $W_{catalog}$ is divided by the approximate source duration f_C^{-1} before plotting in order to obtain the average energy release rate per second. For the aftershocks, we do not apply this division since the source duration of aftershocks is shorter than the time grid interval of 1 s in most cases.

The peaks of the energy release rate capture most of the aftershocks listed in the JMA catalog as concerns both the timing and the amount of energy release. The JMA catalog lists only one aftershock before 200 s, while the obtained energy release rate has many peaks that are missing in the catalog due to its early incompleteness. At least 1 day is usually necessary after a large earthquake to obtain a still incomplete aftershock catalog, while we need only a few tens of seconds for the inversion of the energy release function once the continuous records are provided.

The gray line in Figure 8b represents the linear regression fitting to the energy release rate of 8–16 Hz at the lapse time range of 40–900 s. The line is proportional to $t^{-1.1}$, where t is the lapse time after the main shock. The power exponent of this decay rate is close to the p value of the modified Omori law obtained for several Japanese inland earthquakes [*Enescu et al.*, 2009]. Note that the ordinate of Figure 8b is the cumulative energy radiated by all earthquakes occurring within each time grid interval, rather than the number of events used in the modified Omori law. The cumulative energy has the advantage of not being affected by the early incompleteness of the earthquake catalog. The obtained energy release rate does not show any clear flatting at the lapse time range of 40–900 s, which indicates that the beginning of the power law decay, which is similar to the c value of the modified Omori law, is smaller than 40 s.

Figure 9 shows the spatial distribution of cumulative energy release at the lapse time ranges of 0–10 s, 10–40 s, 40–200 s, and 200–900 s in each frequency range. At 0–10 s, the main shock energy is located near and south of the rupture initiation point (star), which overlaps with the large slip area of the main shock revealed from waveform inversion using 0.1–1 Hz waveform data [*Suzuki et al.*, 2010]. The estimation at 10–40 s may not be good enough according to the synthetic test. At 40–200 s, the energy release is basically located at the west and south subfaults. At 200–900 s, the energy is rather concentrated at the north subfaults. The location of large energy release looks complementary between the lapse time ranges of 0–10 s (main shock) and 40–900 s (early aftershocks). Although the uncertainty is large, this difference could be attributed to the stress transfer and migration of the early aftershocks.

The gray diamonds in Figure 9 represent the location of aftershocks listed in the JMA unified hypocenter catalog. Even though there is only one aftershock listed before 200 s, which is located about 8 km north from the rupture initiation point, the energy release is distributed more widely at the west and south subfaults. At 200–900 s, many listed aftershocks are located north of the rupture initiation point, where the amount of energy release is also large. From these results, we infer that our inversion scheme detects not only the energy release from the events listed in the catalog but also from the events missing in the catalog.

6. Discussions

6.1. On the Stress-Triggering Mechanism of Early Aftershocks

Because conventional waveform inversion using frequencies of less than 1 Hz cannot reveal the termination of the source process precisely, our result obtained at higher frequencies should be more reliable for the detection of the later part of the main shock rupture process. *Kagan and Houston* [2005] commented that the main shock rupture is likely controlled by dynamic stress, while most of the aftershocks are observed at later times when the static stress changes due to the main shock become dominant as the triggering mechanism. Indeed, the velocity amplitude at the borehole bottom of station N.ICWH, which is the closest station to the main shock fault area, is about 1 cm/s at the lapse time of 40 s. The dynamic strain associated with this velocity amplitude is about 4×10^{-6}, which is below the strain threshold above which dynamically triggered earthquakes have been observed [*Gomberg and Johnson*, 2005]. Therefore, the static triggering may be dominant for the aftershocks occurring after the lapse time of 40 s, which is consistent with the estimated energy release rate that follows the power law after 40 s. The transition from the dynamic to the static triggering regime may exist within the lapse times of 10 s to 40 s, which cannot be resolved well through our inversion scheme.
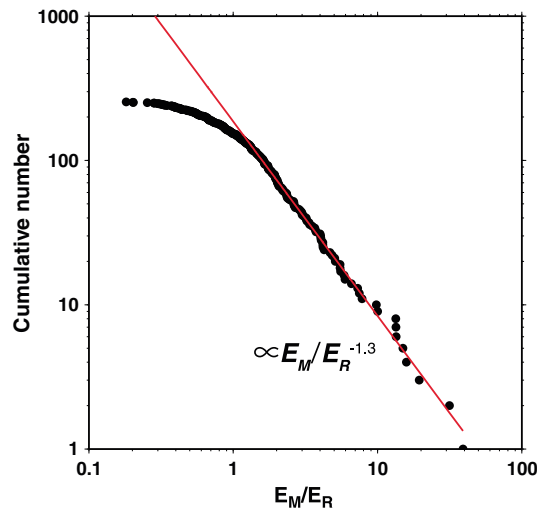
Figure 10. Cumulative number of the maxima of the energy release rate E_M normalized by the average energy decay rate E_R, in the frequency range of 8–16 Hz at the lapse time range of 40–900 s. The regression line (red) is drawn by fitting to the largest 50 normalized maxima.

The locations of large energy release by the early aftershocks (after 40 s) are surrounding that by the main shock. Static stress transfer by the main shock and following aftershocks would be the cause of this spatial complementary relationship. The speed of migration at the early lapse times is important for understanding the physical mechanism of the aftershock triggering [*Lengliné et al.*, 2012] and to forecast the candidate location of large aftershocks. It is necessary to improve the spatial resolution of our inversion scheme for the further interpretation of the migration process.

If a kinematic GPS or a strainmeter is available for the study of "early afterslip" [e.g., *Amoruso and Crescentini*, 2009], the moment release rate and the corresponding stress transfer just after the main shock would be estimated. While the uncertainty is large, *Yokota et al.* [2011] reported a cumulative M_W of 5.5 for the first 600 s afterslip of the Iwate-Miyagi Nairiku earthquake from the analysis of kinematic GPS data. By precisely analyzing the moment release rate together with the energy release rate estimated in this study, we would be able to examine the relationship between the stress transfer and the aftershock excitation. This would constitute a significant progress for the quantification of seismicity using a physics-based modeling.

6.2. On the Early Forecast of Aftershock Activity

Because the energy release rate is estimated within a few tens of seconds after the continuous data are provided, our inversion method would be useful for the early forecasting of aftershock activity. In order to forecast the aftershock activity from the estimated energy release rate in a stochastic manner, we need to quantify the average decay rate of the energy release and the distribution of maxima around the average decay rate in quasi-real time.

We show in Figure 10 the cumulative frequency distribution of E_M/E_R, where the E_M and E_R represent the maxima of energy release rate and the reference energy decay rate shown in Figure 8b, respectively. Note that the maxima do not necessarily correspond to the occurrence of aftershocks because we do not separate the aftershocks that took place at the same time in the inversion. The E_M/E_R distributes following a power law with the exponent -1.3. This power exponent is similar to the b value of the G-R law but is less biased by the threshold of the detection level which varies with lapse time. Once the average energy decay rate and the distribution of maxima are obtained, we would be able to describe the statistics of the aftershock activity. Such information would be available for the early forecasting of aftershock activity [e.g., *Omi et al.*, 2013], without using the aftershock catalog.

The modified Omori law accounts only for the aftershocks triggered by the main shock. The epidemic-type aftershock sequence (ETAS) model [*Ogata*, 1988], on the other hand, was developed based on the concept that "every earthquake can trigger its own aftershocks". Because of its versatility, the ETAS model has been widely applied not only for aftershock forecasting [e.g., *Woessner et al.*, 2011] but also for the evaluation of overall seismicity in the world [e.g., *Ide*, 2013]. Since large aftershocks sometimes trigger significant secondary aftershocks and the seismicity after a large aftershock does not decay smoothly, in general, the ETAS model may be also useful for better accounting for the fluctuation pattern of the energy release rate after the main shock.

6.3. Further Improvement of the Envelope Inversion

Using appropriate envelope Green's function is crucial for the performance of envelope inversion. The theoretical envelope synthesized using equation (2) does not account for the ballistic S wave energy of the

observed envelope well (see Figure 4). Due to this misfit, the location of energy radiation is not well constrained in this study. The primary cause of this misfit is the disregard of forward scattering and radiation pattern of double-couple earthquakes, which affect the ballistic wave energy significantly [e.g., *Sawazaki et al.*, 2011]. To use the envelope synthesized on the basis of the forward scattering approximation [*Sato*, 1989; *Saito et al.*, 2002] would be one possible improvement to be applied. To account for the azimuthal variation of the ballistic wave caused by the radiation pattern, the Monte Carlo simulation proposed by *Sawazaki et al.* [2011] would be useful. In addition, for the purpose of the early forecasting of the aftershock activity, a database of the parameters such as g_0 and Q_i^{-1} must be well prepared in advance.

7. Conclusion

We developed an envelope inversion scheme to reveal the high-frequency (1–16 Hz) energy release process of the main shock and the early aftershock sequence. According to this scheme, the main shock and the early aftershocks are regarded as a continuous energy release process, and the centroid of the energy release is estimated at each time node using continuous seismogram records of Hi-net and KiK-net. The scattered energy that contaminated in the seismogram envelope is deconvolved well unless the energy release rate decreases too suddenly. The peaks of the estimated energy release mostly coincide with the timing and magnitude of the aftershocks listed in the JMA unified hypocenter catalog. We also detect many peaks in the estimated energy release rate that do not have corresponding event in the JMA catalog. The seismic energy is released following the temporal decay rate of $t^{-1.1}$ at 40–900 s after the main shock, which is similar to the modified Omori law. The area of high-frequency energy release is located near and south of the rupture initiation point of the main shock at the lapse times of 0–10 s, which overlaps the large slip area of the main shock. At the lapse times after 40 s, the location of energy radiation is distributed more widely surrounding the area of large energy release by the main shock. A size distribution similar to the Gutenberg-Richter law also holds for the normalized maxima of the obtained energy release rate. In this study, we have demonstrated the usage of the high-sensitivity dense continuous seismogram records that can capture the main characteristics of early aftershocks. By applying the proposed inversion method to many main shock-aftershock sequences, we would be able to capture the temporal and spatial patterns of early aftershocks, which will be useful for the study of the triggering mechanism of the aftershocks and for the early forecasting of seismicity.

References

Abubakirov, I. R. (2005), Attenuation characteristics of transverse waves in the lithosphere of Kamchatka estimated from observations at the Petropavlovsk digital broadband station, *Izv. Phys. Solid Earth*, *41*(10), 813–824.

Aki, K. (1967), Scaling law of seismic spectrum, *J. Geophys. Res.*, *72*(4), 1217–1231, doi:10.1029/JZ072i004p01217.

Amoruso, A., and L. Crescentini (2009), Slow diffusive fault slip propagation following the 6 April 2009 L'Aquila earthquake, Italy, *Geophys. Res. Lett.*, *36*, L24306, doi:10.1029/2009GL041503.

Aoi, S., T. Kunugi, and H. Fujiwara (2008), Trampoline effect in extreme ground motion, *Science*, *322*(5902), 727–730, doi:10.1126/science.1163113.

Baltay, A., S. Ide, G. Prieto, and G. Beroza (2011), Variability in earthquake stress drop and apparent stress, *Geophys. Res. Lett.*, *38*, L06303, doi:10.1029/2011GL046698.

Brune, J. N. (1970), Tectonic stress and the spectra of seismic shear waves from earthquakes, *J. Geophys. Res.*, *75*(26), 4997–5009, doi:10.1029/JB075i026p04997.

Calvet, M., and L. Margerin (2013), Lapse-time dependence of coda Q: Anisotropic multiple-scattering models and application to the Pyrenees, *Bull. Seismol. Soc. Am.*, *103*(3), 1993–2010, doi:10.1785/0120120239.

Carcolé, E., and H. Sato (2010), Spatial distribution of scattering loss and intrinsic absorption of short-period S waves in the lithosphere of Japan on the basis of the multiple lapse time window analysis of Hi-net data, *Geophys. J. Int.*, *180*(1), 268–290, doi:10.1111/j.1365-246X.2009.04394.x.

Dieterich, J. (1994), A constitutive law for rate of earthquake production and its application to earthquake clustering, *J. Geophys. Res.*, *99*(B2), 2601–2618, doi:10.1029/93JB02581.

Enescu, B., J. Mori, and M. Miyazawa (2007), Quantifying early aftershock activity of the 2004 mid-Niigata Prefecture earthquake (M_W6.6), *J. Geophys. Res.*, *112*, B04310, doi:10.1029/2006JB004629.

Enescu, B., J. Mori, M. Miyazawa, and Y. Kano (2009), Omori-Utsu law c-values associated with recent moderate earthquakes in Japan, *Bull. Seismol. Soc. Am.*, *99*(2A), 884–891, doi:10.1785/0120080211.

Eshelby, J. D. (1957), The determination of the elastic field of an ellipsoidal inclusion, and related problems, *Proc. R. Soc. London, Ser. A*, *241*(1226), 376–396, doi:10.1098/rspa.1957.0133.

Fehler, M., M. Hoshiba, H. Sato, and K. Obara (1992), Separation of scattering and intrinsic attenuation for the Kanto-Tokai region, Japan, using measurements of S-wave energy versus hypocentral distance, *Geophys. J. Int.*, *108*(3), 787–800, doi:10.1111/j.1365-246X.1992.tb03470.x.

Gomberg, J., and P. Johnson (2005), Dynamic triggering of earthquakes, *Nature*, *437*(7060), 830, doi:10.1038/437830a.

Gusev, A. A. (1995), Vertical profile of turbidity and coda Q, *Geophys. J. Int.*, *123*(3), 665–672, doi:10.1111/j.1365-246X.1995.tb06882.x.

Gusev, A. A., and V. M. Pavlov (1991), Deconvolution of squared velocity waveform as applied to the study of a noncoherent short-period radiator in the earthquake source, *Pure Appl. Geophys.*, *136*(2–3), 235–244, doi:10.1007/BF00876375.

Ide, S. (2013), The proportionality between relative plate velocity and seismicity in subduction zones, *Nat. Geosci.*, *6*(9), 780–784, doi:10.1038/ngeo1901.

Ishii, M., P. M. Shearer, H. Houston, and J. E. Vidale (2005), Extent, duration and speed of the 2004 Sumatra–Andaman earthquake imaged by the Hi-Net array, *Nature*, *435*(7044), 933–936, doi:10.1038/nature03675.

Kagan, Y. Y. (2004), Short-term properties of earthquake catalogs and models of earthquake source, *Bull. Seismol. Soc. Am.*, *94*(4), 1207–1228, doi:10.1785/012003098.

Kagan, Y. Y., and H. Houston (2005), Relation between mainshock rupture process and Omori's law for aftershock moment release rate, *Geophys. J. Int.*, *163*(3), 1039–1048, doi:10.1111/j.1365-246X.2005.02772.x.

Kakehi, Y., and K. Irikura (1996), Estimation of high-frequency wave radiation areas on the fault plane by the envelope inversion of acceleration seismograms, *Geophys. J. Int.*, *125*(3), 892–900, doi:10.1111/j.1365-246X.1996.tb06032.x.

Kanamori, H. (1977), The energy release in great earthquakes, *J. Geophys. Res.*, *82*(20), 2981–2987, doi:10.1029/JB082i020p02981.

Kiser, E., and M. Ishii (2013), Hidden aftershocks of the 2011 M_W 9.0 Tohoku, Japan earthquake imaged with the backprojection method, *J. Geophys. Res. Solid Earth*, *118*, 5564–5576, doi:10.1002/2013JB010158.

Lengliné, O., B. Enescu, Z. Peng, and K. Shiomi (2012), Decay and expansion of the early aftershock activity following the 2011, M_W9.0 Tohoku earthquake, *Geophys. Res. Lett.*, *39*, L18309, doi:10.1029/2012GL052797.

Mayeda, K., R. Gök, W. R. Walter, and A. Hofstetter (2005), Evidence for non-constant energy/moment scaling from coda-derived source spectra, *Geophys. Res. Lett.*, *32*, L10306, doi:10.1029/2005GL022405.

Nakahara, H. (2008), Seismogram envelope inversion for high-frequency seismic energy radiation from moderate to large earthquakes, in *Earth Heterogeneities and Scattering Effects on Seismic Waves*, Advanced in Geophysics (Series Ed. R. Dmowska), vol. 50, edited by H. Sato and M. C. Fehler, pp. 401–426, Academic Press, Amsterdam, Netherlands.

Nakahara, H., T. Nishimura, H. Sato, and M. Ohtake (1998), Seismogram envelope inversion for the spatial distribution of high-frequency energy radiation from the earthquake fault: Application to the 1994 far east off Sanriku earthquake, Japan, *J. Geophys. Res.*, *103*(B1), 855–867, doi:10.1029/97JB02676.

Obara, K., K. Kasahara, S. Hori, and Y. Okada (2005), A densely distributed high-sensitivity seismograph network in Japan: Hi-net by National Research Institute for Earth Science and Disaster Prevention, *Rev. Sci. Instrum.*, *76*(2), 021,301, doi:10.1063/1.1854197.

Ogata, Y. (1988), Statistical models for earthquake occurrences and residual analysis for point processes, *J. Am. Stat. Assoc.*, *83*(401), 9–27, doi:10.1080/01621459.1988.10478560.

Ohta, Y., M. Ohzono, S. Miura, T. Iinuma, K. Tachibana, K. Takatsuka, K. Miyao, T. Sato, and N. Umino (2008), Coseismic fault model of the 2008 Iwate-Miyagi Nairiku earthquake deduced by a dense GPS network, *Earth Planets Space*, *60*(12), 1197–1201.

Omi, T., Y. Ogata, Y. Hirata, and K. Aihara (2013), Forecasting large aftershocks within one day after the main shock, *Sci. Rep.*, *3*, 2218, doi:10.1038/srep02218.

Oth, A., D. Bindi, S. Parolai, and D. Di Giacomo (2010), Earthquake scaling characteristics and the scale-(in) dependence of seismic energy-to-moment ratio: Insights from KiK-net data in Japan, *Geophys. Res. Lett.*, *37*, L19304, doi:10.1029/2010GL044572.

Paasschens, J. C. J. (1997), Solution of the time-dependent Boltzmann equation, *Phys. Rev. E*, *56*(1), 1135–1141, doi:10.1103/PhysRevE.56.1135.

Peng, Z., and P. Zhao (2009), Migration of early aftershocks following the 2004 Parkfield earthquake, *Nat. Geosci.*, *2*(12), 877–881, doi:10.1038/NGEO697.

Peng, Z., J. E. Vidale, and H. Houston (2006), Anomalous early aftershock decay rate of the 2004 Mw6.0 Parkfield, California, earthquake, *Geophys. Res. Lett.*, *33*, L17307, doi:10.1029/2006GL026744.

Peng, Z., J. E. Vidale, M. Ishii, and A. Helmstetter (2007), Seismicity rate immediately before and after main shock rupture from high-frequency waveforms in Japan, *J. Geophys. Res.*, *112*, B03306, doi:10.1029/2006JB004386.

Phillips, W. S., and K. Aki (1986), Site amplification of coda waves from local earthquakes in central California, *Bull. Seismol. Soc. Am.*, *76*(3), 627–648.

Saito, T., H. Sato, and M. Ohtake (2002), Envelope broadening of spherically outgoing waves in three-dimensional random media having power law spectra, *J. Geophys. Res.*, *107*(B5), 2089, doi:10.1029/2001JB000264.

Sato, H. (1989), Broadening of seismogram envelopes in the randomly inhomogeneous lithosphere based on the parabolic approximation: Southeastern Honshu, Japan, *J. Geophys. Res.*, *94*(B12), 17,735–17,747, doi:10.1029/JB094iB12p17735.

Sawazaki, K., H. Sato, and T. Nishimura (2011), Envelope synthesis of short-period seismograms in 3-D random media for a point shear dislocation source based on the forward scattering approximation: Application to small strike-slip earthquakes in southwestern Japan, *J. Geophys. Res.*, *116*, B08305, doi:10.1029/2010JB008182.

Shiomi, K., K. Obara, and K. Kasahara (2005), Amplitude saturation of the NIED Hi-net waveforms and simple criteria for recognition [in Japanese], *Zisin2*, *57*, 451–461.

Suzuki, W., S. Aoi, and H. Sekiguchi (2010), Rupture process of the 2008 Iwate-Miyagi Nairiku, Japan, Earthquake derived from near-source strong-motion records, *Bull. Seismol. Soc. Am.*, *100*(1), 256–266, doi:10.1785/0120090043.

Takemoto, T., T. Furumura, T. Saito, T. Maeda, and S. Noguchi (2012), Spatial- and frequency-dependent properties of site amplification factors in Japan derived by the coda normalization method, *Bull. Seismol. Soc. Am.*, *102*(4), 1462–1476, doi:10.1785/0120110188.

Utsu, T. (1961), A statistical study on the occurrence of aftershocks, *Geophys. Mag.*, *30*, 521–605.

Woessner, J., S. Hainzl, W. Marzocchi, M. J. Werner, A. M. Lombardi, F. Catalli, B. Enescu, M. Cocco, M. C. Gerstenberger, and S. Wiemer (2011), A retrospective comparative forecast test on the 1992 Landers sequence, *J. Geophys. Res.*, *116*, B05305, doi:10.1029/2010JB007846.

Yokota, Y., K. Koketsu, and T. Kato (2011), Detection and analysis of early afterslip following the 2008 Iwate-Miyagi Nairiku, Japan, earthquake, abstract of Japan Geoscience Union Meeting, SSS025-P01.

Zeng, Y., F. Su, and K. Aki (1991), Scattering wave energy propagation in a random isotropic scattering medium 1. Theory, *J. Geophys. Res.*, *96*(B1), 607–619, doi:10.1029/90JB02012.